Time-dependent density-functional-theory study of the suppressed tunneling ionization of vanadium

Xi Chu
Department of Chemistry and Biochemistry, University of Montana, Missoula, Montana 59812, USA

Gerrit C. Groenenboom
Institute for Molecules and Materials, Radboud University Nijmegen, Heyendaalseweg 135, 6525 AJ Nijmegen, The Netherlands

(Received 26 August 2016; published 21 November 2016)

Using a time-dependent density-functional-theory (TDDFT) method that incorporates the exact exchange, we reproduce the measured ionization suppression for vanadium in 1500-nm lasers of 1.4 to 2.8 $\times 10^{13}$ W/cm^2. The calculated ionization yields are 0.07 to 0.5 in 100 fs sin^2 pulses. For weaker laser intensities a method with more configurations is needed to properly describe the multiphoton, rather than tunneling, ionization of a transition-metal atom. Our calculations show that the isotropic component of the induced potential increases the binding energy of the electron while the dipole component elevates the potential barrier of tunneling ionization. Both effects suppress the tunneling ionization.

DOI: 10.1103/PhysRevA.94.053417

I. INTRODUCTION

The rapid advance in attosecond science [1,2] offers the possibility of probing or even controlling the electronic structure with subfemtosecond and sub-ångström resolution using intense pulsed lasers. Ionization is a prominent phenomenon in intense laser fields and its understanding has been mostly based on the single-active-electron (SAE) approximation. The Ammosov-Delone-Krainov (ADK) approximation [3] is a widely adopted SAE model for tunneling ionization. Experiments showed, however, that the tunneling ionization yields for transition-metal atoms V, Ni, Pd, Ta, and Nb are significantly lower than the ADK predictions [4,5]. It was proposed that the multielectron response exerts an additional barrier for tunneling ionization [5]. Core polarization was subsequently included into a tunneling model [6–8]. The induced dipole moment of the ion was considered to increase the ionization barrier.

However, as the electrons move away from the nucleus in a laser field, an isotropic attractive potential is expected at the core. It reduces, rather than increases, the potential barrier of the ionization. The role of this induced attractive potential has not been discussed.

Solutions of time-dependent (TD) Schrödinger equations would provide a rigorous description of the relation between multielectron effects and the ionization suppression. Such solutions for transition-metal atoms, however, remain challenging. For similar reasons, modeling transition-metal chemistry has largely relied on density functional theory (DFT), even though the ground-state wave function of an open-shell atom may not be represented by a single determinant. Using DFT one must find a reference single determinant that renders the electron density of the ground state. In this study on the strong-field ionization of vanadium, we will demonstrate that TDDFT calculations can reproduce the measured ionization yields for a range of laser intensity, using which we will analyze the main cause of the ionization suppression.

The electronic configuration and term symbol for the neutral vanadium are $3d^34s^2$ and $^4F_{3/2}$, respectively. There are four degenerate states with total angular momentum projection quantum numbers $M_J = \pm 1/2$ or $\pm 3/2$, none of which is representable by a single determinant. The fine structure level $^4F_{9/2}$ is 0.068 558 eV above the ground state [9] and the states with $M_J = \pm 9/2$ can both be presented by a single determinant. We will calculate the ionization rate for these states and use it as an approximation of the rate for the electronic configuration $3d^34s^2$.

Similar approximations were made for determining the polarizability and its anisotropy for transition metals [10,11] and rare-earth metals [12] by a linear response TDDFT. In these studies reasonable accuracy was achieved for open-shell atoms that have partially filled d or f subshells. Our nonperturbative version of TDDFT was benchmarked for strong-field ionization of diatomic molecules [13]. It also describes two electron processes in the high harmonic generation of H_2 [14] and N_2 [15,16]. Here, using vanadium as an example, we extend the TDDFT method to treat open-shell atoms nonperturbatively.

As in the earlier work, we implement the TDDFT as a set of TD Kohn-Sham equations, which in principle includes many-body effects through a local TD exchange-correlation (XC) potential. We consider a quantum action integral [17–19],

$$A[\Psi] = \int_{t_0}^{t_1} dt \langle \Psi(t)| i\frac{\partial}{\partial t} - \hat{H}(t)|\Psi(t)\rangle, \tag{1}$$

where $\Psi(t)$ is the total N-electron wave function and it is represented by the determinant,

$$\Psi(t) = \frac{1}{\sqrt{N!}} \det[\psi_{1\sigma}(t)\psi_{2\sigma}(t)\ldots\psi_{N\sigma}(t)], \tag{2}$$

where σ is the spin index. The electron spin density at time t is determined by the set of occupied orbitals $\{\psi_{i\sigma}\}$ as

$$\rho_\sigma(\boldsymbol{r},t) = \sum_{i=1}^{N_\sigma} \psi_{i\sigma}^*(\boldsymbol{r},t)\psi_{i\sigma}(\boldsymbol{r},t), \tag{3}$$

where i is the orbital index. The quantum action $A[\Psi]$ has a stationary point at the TD density of the system, and hence from the Euler equation we get the working equations [20,21].

When we project Eq. (2) onto a determinant of field free orbitals we find contributions of single, double, triple, and higher excitations. Such multiple excitations or de-excitations are needed for simulating transition metals.

The exchange and correlation potential is crucial for the accuracy of a TDDFT method. To correctly account for the long-range singularity and the anisotropy of an open-shell atom, we implement an optimized effective potential formalism.

II. KOHN-SHAM EQUATIONS WITH AN OPTIMIZED EFFECTIVE POTENTIAL FOR OPEN SHELL ATOMS

The optimized effective potential (OEP) approach of Sharp and Horton [22] consists of a set of one-electron equations, in atomic units,

$$\left[-\frac{1}{2}\nabla^2 + V_\sigma^{\mathrm{OEP}}(\mathbf{r})\right]\phi_{i\sigma}(\mathbf{r}) = \varepsilon_{i\sigma}\phi_{i\sigma}(\mathbf{r}), \quad (i = 1,2,\ldots,N_\sigma), \tag{4}$$

in which N_σ is the number of electrons for the σ spin and $V_\sigma^{\mathrm{OEP}}(\mathbf{r})$ minimizes the total energy $E[\{\phi_{i\uparrow},\phi_{j\downarrow}\}]$, i.e.,

$$\frac{\delta E}{\delta V_\sigma^{\mathrm{OEP}}} = 0. \tag{5}$$

Krieger *et al.* developed a semianalyic transform of the OEP equations [23]. Adopting a similar seminanalytic form of the OEP equations, we incorporate the exact exchange energy

$$E_x = -\frac{1}{2}\sum_\sigma\sum_{i,j}\iiint d^3\mathbf{r}\iint \times \int d^3\mathbf{r}'\frac{\phi_{i\sigma}^*(\mathbf{r}')\phi_{j\sigma}^*(\mathbf{r})\phi_{j\sigma}(\mathbf{r}')\phi_{i\sigma}(\mathbf{r})}{|\mathbf{r}-\mathbf{r}'|} \tag{6}$$

into the Kohn-Sham (KS) equations,

$$\hat{H}_\sigma^0(\mathbf{r})\phi_{i\sigma}(\mathbf{r}) = \varepsilon_{i\sigma}\phi_{i\sigma}(\mathbf{r}), \tag{7}$$

where

$$\hat{H}_\sigma^0(\mathbf{r}) = -\frac{1}{2}\nabla^2 - \frac{Z}{r} + \iiint\frac{\rho(\mathbf{r}')}{|\mathbf{r}-\mathbf{r}'|}d^3\mathbf{r}' + V_{\mathrm{xc},\sigma}(\mathbf{r}), \tag{8}$$

$$\rho(\mathbf{r}) = \rho_\uparrow(\mathbf{r}) + \rho_\downarrow(\mathbf{r}), \tag{9}$$

in which Z is the nuclear charge, r is the radial distance to the nucleus, and

$$\rho_\sigma(\mathbf{r}) = \sum_i^{N_\sigma}|\phi_{i\sigma}(\mathbf{r})|^2. \tag{10}$$

The orbital independent local exchange-correlation potential is approximated by

$$V_{\mathrm{xc},\sigma}(\mathbf{r}) = \frac{\delta E_{\mathrm{xc}}[\rho_\uparrow,\rho_\downarrow]}{\delta\rho_\sigma(\mathbf{r})} \approx \frac{1}{\rho_\sigma(\mathbf{r})}\sum_i|\phi_{i\sigma}(\mathbf{r})|^2\left[v_{x,i\sigma}(\mathbf{r}) + v_{c,i\sigma}(\mathbf{r}) + \bar{V}_{\mathrm{xc},\sigma}^i\right], \tag{11}$$

where the orbital dependent exchange potential is

$$v_{x,i\sigma}(\mathbf{r}) = \frac{1}{\phi_{i\sigma}^*(\mathbf{r})}\frac{\delta E_x}{\delta\phi_{i\sigma}(\mathbf{r})} \tag{12}$$

TABLE I. Orbital energies of V calculated by the OEP method.

Electronic configuration of the ion	Level	I_p (eV) [9]	Orbital	$-\epsilon(eV)$
$3d^3 4s$	$^5F_5$	7.07	$4s_\downarrow$	6.99
$3d^3(^4F)4s$	$^3F_4$	7.81	$4s_\uparrow$	7.69
$3d^2 4s^2$	$^3F_4$	11.45	$3d_\uparrow$	11.42

and $v_{c,i\sigma} = \frac{1}{\phi_{i\sigma}^*(\mathbf{r})}\frac{\delta E_c^{cs}}{\delta\phi_{i\sigma}(\mathbf{r})}$ is the correlation potential derived from the energy functional formulated by Colle and Salvetti [24]. The constant is obtained as

$$\bar{V}_{\mathrm{xc},\sigma}^i = \langle\psi_{i\sigma}|V_{\mathrm{xc},\sigma}(\mathbf{r}) - v_{x,i\sigma}(\mathbf{r}) - v_{c,i\sigma}^{cs}(\mathbf{r})|\psi_{i\sigma}\rangle \tag{13}$$

for occupied orbitals other than the highest. For the highest occupied orbitals, we replace $\bar{V}_{\mathrm{xc},\sigma}^i$ by a function of r, which is set to be zero at infinity, so that the negative of the orbital energy reproduces the ionization potential (IP).

To solve Eq. (7), we use the generalized pseudospectral method [25] that puts more grid points near the nucleus and fewer near the cutoff, which is at 1000 a_0. An absorbing boundary is placed at 75 a_0. There are five adjustable parameters in the static OEP code, the maximum radial distance, the absorbing boundary, the number of grid points, the number of partial waves, and a mapping parameter. We obtained convergence with respect to all five. Table I shows the calculated orbital energies together with the measured IPs for removing an electron from the orbital.

III. IONIZATION YIELDS

To obtain the ionization yields, we solve the time-dependent equations

$$i\frac{\partial}{\partial t}\psi_{i\sigma}(\boldsymbol{r},t) = \hat{H}_\sigma(\boldsymbol{r})\psi_{i\sigma}(\boldsymbol{r},t) = \left[\hat{H}_\sigma^0(\boldsymbol{r}) + \Delta\hat{V}_\sigma(\boldsymbol{r},t)\right]\psi_{i\sigma}(\boldsymbol{r},t), \quad i = 1,2,\ldots,N_\sigma, \tag{14}$$

where

$$\Delta\hat{V}_\sigma(\boldsymbol{r},t) = \iiint\frac{\Delta\rho(\mathbf{r}',t)}{|\mathbf{r}-\mathbf{r}'|}d^3\boldsymbol{r}' + \Delta V_{\mathrm{xc},\sigma}(\boldsymbol{r},t) - \boldsymbol{E}(t)\cdot\boldsymbol{z} \tag{15}$$

and $\boldsymbol{E}(t) = E(t)\hat{\boldsymbol{z}}$ is the electric field of the laser, $|\hat{z}| = 1$. $\Delta\rho$ is the change of the electron density at time t relative to time 0, i.e.,

$$\Delta\rho(\boldsymbol{r},t) = \rho_\uparrow(\boldsymbol{r},t) + \rho_\downarrow(\boldsymbol{r},t) - \rho(\boldsymbol{r}), \tag{16}$$

in which $\rho_\sigma(\mathbf{r},t)$ and $\rho(\mathbf{r})$ are given in Eqs. (3) and (9) respectively. The change in the exchange-correlation potential, ΔV_{xc}, is

$$\Delta V_{\mathrm{xc},\sigma}(\boldsymbol{r},t) = V_{\mathrm{xc},\sigma}(\boldsymbol{r},t) - V_{\mathrm{xc},\sigma}(\boldsymbol{r}), \tag{17}$$

where $V_{\mathrm{xc},\sigma}(\boldsymbol{r})$ is given in Eq. (11) and $V_{\mathrm{xc},\sigma}(\boldsymbol{r},t)$ is obtained by using the adiabatic approximation [18,27], $v_{\mathrm{xc},\sigma}(\boldsymbol{r},t) = v_{\mathrm{xc},\sigma}[\rho_\sigma(\boldsymbol{r},t)]$, i.e., replacing ρ_σ, and subsequently $\phi_{i\sigma}$, by the corresponding time-dependent quantities in Eq. (11).

While the rates for peak intensities are very different than the rates for the average intensity over the pulse, the total yields and their trends when plotted against the peak intensity vary only slightly with respect to the pulse duration and shape. A $\sin^2$ pulse shape of 20 optical cycles is assumed in our calculations.

We use the time-dependent generalized pseudospectral method to solve Eq. (14). For comparison with the measurements by Smits *et al.* [5], we first calculate the survival probability for each spin orbital as

$$n_{i\sigma} = \iiint \psi^*_{i\sigma}(\mathbf{r},T)\psi_{i\sigma}(\mathbf{r},T)d^3\mathbf{r}, \tag{18}$$

where T is the pulse length and the ionization probability for each spin orbital as

$$\gamma_{i\sigma} = 1 - n_{i\sigma}. \tag{19}$$

We have verified that the pulse length and pulse shape have little influence on the ionization yield P,

$$P = 1 - \prod_{i\sigma} n_{i\sigma} + 2 \sum_{i\sigma_1 \neq j\sigma_2} \gamma_{i\sigma_1}\gamma_{j\sigma_2} \prod_{k\sigma_3 \neq i\sigma_1}^{k\sigma_3 \neq j\sigma_2} n_{k\sigma_3}, \tag{20}$$

in which both the single and double ionization is included.

IV. RESULTS AND DISCUSSION

The electronic configurations for the neutral and cationic vanadium are $3d^34s^2$ and $3d^4$, respectively. As such, the ground-state configuration of the ion cannot be reached through a single electron process. Table I shows that the energy for removing a single active electron while keeping other electrons in their atomic orbitals is higher than 6.75 eV, the IP for reaching the ground state of the ion.

To estimate the effect of a higher ionic state, we first calculate the ADK tunneling yields for different ionization potentials. Figure 1 shows ADK curves for three IPs. Corresponding electronic configurations of the ion are give in Table I. For comparison, we also adopted an independent electron method, for which we replace Eq. (15) by its last term

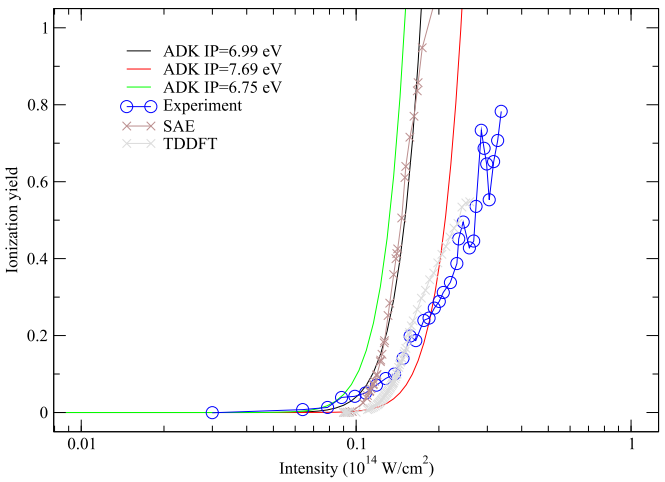

FIG. 1. Ionization yield of vanadium in 1500-nm lasers as a function of the laser intensity.

only and solve Eq. (14). The electrons are subject to the electric field of the laser and the attractive potential of the ion, which is held constant in the propagation. Even though we include all the occupied spin orbitals in the propagation, only the highest contributes significantly to ionization. Since it is assumed that the potential from the ion does not change with time, it is a form of the SAE approximation and it is labeled as such in Fig. 1. When the intensity is greater than 1.26×10^{13} W/cm^2, the ionization yields predicted by this approximation are remarkably close to the ADK predictions with the ionization potential set to be 6.99 eV. The electronic configuration of the ion is $3d^34s$ for this potential. At 1.26×10^{13} W/cm^2, the Keldysh parameter is 1.15 for the 1500-nm lasers. It indicates that the ionization is not tunneling dominant at this intensity or lower, which explains the difference with the ADK tunneling model.

In Fig. 1 we also plot the experimental values from Ref. [5]. At larger intensities, they are significantly lower than the ADK values with 6.99 eV being the ionization potential. It is also lower than our SAE values. This comparison confirms that the slightly increased ionization potential associated with the SAE approximation does not cause the ionization suppression.

Using our TDDFT method, which includes the dynamics of the ion, the ionization yields become reasonably close to the experimental values. It shows that the many electron dynamics according to the TDDFT formalism reproduces the suppression of ionization for intensities greater than 1.4×10^{13} W/cm^2. Due to the limitation of the local adiabatic XC potential [26], the atom cannot be too far away from the ground state [28]. We therefore focus on yields that are less than 0.5, which should be most reliable.

To analyze the many electron effects, we rewrite Eq. (15) as

$$\Delta\hat{V}_\sigma(\boldsymbol{r},t) = -\boldsymbol{E}(t)\cdot\boldsymbol{z} + \sum_{l=0}^{\infty} \Delta v_{\sigma,l}(r,t)P_l(z/r), \tag{21}$$

where P_l is lth-order Legendre function and z is the z coordinate. Induced potentials $\Delta v_{\sigma,l}P_l$, $l = 0,1,\ldots,\infty$ contain all the dynamic many-electron effects. The zeroth-order term $\Delta v_{\sigma,0}$ is isotropic. The first-order term ($l = 1$) is associated with the induced dipole moment for larger radial distances, and the second-order term with the induced quadrupole moment.

In Fig. 2 we plot $\Delta v_{\downarrow,l}P_l$ along the z axis for $l = 0,1$, and 2, when the laser intensity is 1.54×10^{13} W/cm^2 and the field strength is maximized, i.e., $t = T/2$. We choose the spin $\downarrow$, because $4s_\downarrow$ is the highest spin orbital according to our convention (see Table I). The ionization yield predicted by TDDFT agrees well with the measurement for this intensity (see Fig. 1).

Figure 2 shows that the second-order contribution, i.e., $\Delta v_{\downarrow,2}P_2$, is small and the contribution of higher orders are even smaller since they require more photons. The first-order induced potential peaks at 2.6 bohr and 0.07 hartree. It elevates the ionization barrier and reduces the tunneling ionization rate. The zeroth-order induced potential is attractive as a result of the electrons moving away from the nucleus in the electric field of the laser. It lowers the energy of the highest electron dynamically and creates a larger time-dependent ionization potential. This effect is demonstrated in Fig. 3.

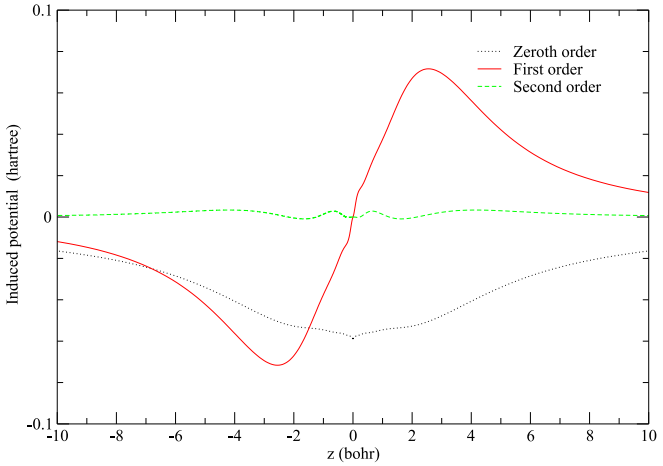

FIG. 2. Induced potential, $\Delta v_{\downarrow,l} P_l$, $l = 0,1,2$, at the peak intensity of 1.54×10^{13} W/cm^2, 1500-nm laser.

The red (gray) and back lines in Fig. 3 show the energy level and potentials with and without considering the many-body effects, respectively. The black dash-dotted line is the field free electronic potential expressed as the sum of the last three terms in Eq. (8). These three terms are added to the potential from the electric field of the laser $-\boldsymbol{E}(T/2)\cdot z$ and plotted as the black dotted line. The black solid line is the energy of the highest occupied spin orbital. It is above the potential barrier; therefore the ionization yield would be high if the many-electron effect is excluded.

With the isotropic induced potential added to the field free electronic potential (dashed red [gray] line in Fig. 3), the energy level is shifted to the red (gray) solid line. The double dotted red (gray) dashed line shows the electronic potential at $T/2$ along the z axis with all terms of the induced potential included. Comparing the energy level and potential, we see tunneling ionization, whose rate turns out to be much lower than over the barrier ionization rates. We found similar features as shown in Fig. 3 for intensities up to 3×10^{13} W/cm^2.

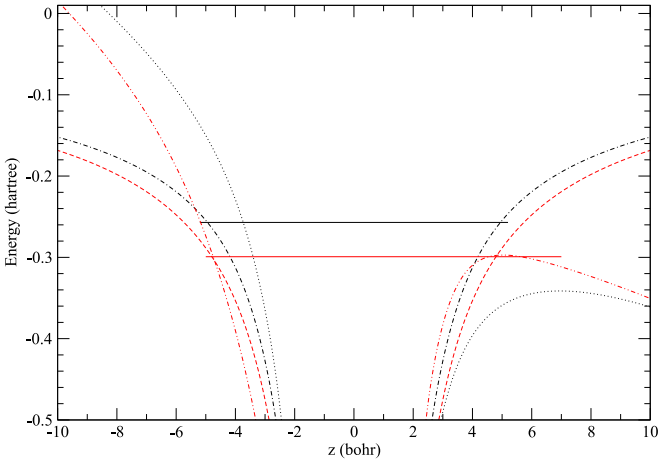

FIG. 3. Energy diagram for vanadium in a 1500-nm laser of 1.54×10^{13} W/cm^2. Dot-dashed black line: the field free electronic potential along the z axis. Solid black line: the field free energy level for the highest occupied spin orbital. Black dotted line: the potential of the electric field at the peak intensity plus the field free electronic potential. Red (gray) dashed line: the shifted electronic potential due to the even order responses of the electrons at the peak intensity. Red (gray) solid line: the lowered energy level corresponding to the red (gray) dashed line. Dashed double dotted red (gray) line: the electronic potential at the peak intensity according to our TDDFT formalism.

In the introduction we explained that we performed calculations for the $^4F_{9/2}$ fine structure level, which is 0.068 558 eV above the $J = 3/2$ ground state. The $M_J = 9/2$ state, with orbital angular momentum quantum numbers $L = 3, M_L = 3$ and electron spin quantum numbers $S = 3/2, M_S = 3/2$ can be represented by a single determinant, $D_1 = |3d_0\, 3d_1\, 3d_2|$, where only the $3d$ spin orbitals are included in the notation and spin-up and spin-down orbitals with magnetic quantum numbers m are written as $3d_m$ and $\overline{3d}_m$, respectively. In general, the $^4F_{J,M_J}$ states are linear combinations of Russell-Saunders microstates $|LM_LSM_S\rangle$ with $L = 3$, $S = 3/2$, and $M_J = M_L + M_S$:

$$|^4F_{J,M_J}\rangle = \sum_{M_L=-L}^{L} \sum_{M_S=-S}^{S} |LM_LSM_S\rangle\langle LM_LSM_S|JM_J\rangle,$$

where the expansion coefficients are Clebsch-Gordan coefficients. The dominant microstate contributing to the $^4F_{3/2,3/2}$ ground state has $M_L = 3$ and $M_S = -3/2$; its contribution is $|\langle 3,3,3/2,-3/2|3/2,3/2\rangle|^2 \approx 57\%$. This microstate can be represented by a single determinant, $D_2 = |\overline{3d}_0\, \overline{3d}_1\, \overline{3d}_2|$. Since spin-orbit coupling is not included, the results of the calculations are the same for states represented by D_1 and D_2. A better approximation of the ground state would require microstates with $|M_LM_S\rangle = |2,-1/2\rangle$ (≈29%), $|M_LM_S\rangle = |1,1/2\rangle$ (≈11%), and $|M_LM_S\rangle = |0,3/2\rangle$ (≈3%). We currently cannot use multiple determinants in our method, but in a variational approach doing so would result in stronger binding of the electron, which could improve the predicted ionization probability for laser intensities lower than 1.3×10^{13} W/cm^2. For higher intensities, we hypothesize that similar shifts of energy levels and electronic potentials as shown in Fig. 3 cause the suppression of ionization of the $^4F_{3/2}$ level. We used a few of the determinants that contribute to $|M_LM_S\rangle = |2,-1/2\rangle$ and $|M_LM_S\rangle = |1,1/2\rangle$ as initial input for the TD equations with laser parameters specified for Fig. 3. Each calculation results in curves slightly different than those shown in Fig. 3, but all show downward-shifted energy levels and upward-shifted energy barriers due to many electron interactions. We will further study the relationship between the initial configuration and strong-field ionization of transition metals with this method.

V. CONCLUSIONS

We developed a TDDFT method that incorporates the exact exchange and used it to investigate the ionization of vanadium in intense 1500-nm lasers. The experimental results are reproduced in the intensity range of 1.3 to 2.8×10^{13} W/cm^2. The corresponding ionization yields are 0.07 to 0.55 in 20 optical cycle pulses.

For intensities lower than 1.3×10^{13} W/cm^2, the measured values appear to be higher than our predictions. It suggests

that properly describing the electron correlation may be particularly important for calculating ionization rates at lower intensities, because electron correlation reduces the ionization potential for vanadium and thus enhances the ionization. A method that includes more than one configuration may be needed.

Dynamic many-electron interactions substantially lower the ionization yields. Our calculations show that as the electrons move away from the nucleus in an intense laser field of 1.3 to 2.8×10^{13} W/cm^2, the induced isotropic potential is attractive and hence increases the spontaneous ionization potential and reduces the ionization rate. The induced dipole moment elevates the ionization barrier and reduces the ionization rate. Both effects make substantial contributions.

ACKNOWLEDGMENTS

This work is supported by the National Science Foundation Award No. PHY-1506441.

[1] R. Kienberger, M. Hentschel, M. Uiberacker, C. Spielmann, M. Kitzler, A. Scrinzi, M. Wieland, T. Westerwalbesloh, U. Kleineberg, U. Heinzmann *et al.*, Science **297**, 1144 (2002).
[2] F. Krausz and M. Ivanov, Rev. Mod. Phys. **81**, 163 (2009).
[3] M. V. Ammosov, N. B. Delone, and V. P. Kraĭnov, Zh. Eksp. Teor. Fiz. **91**, 2008 (1986) [Sov. Phys. JETP **64**, 1191 (1986)].
[4] M. Lezius, V. Blanchet, M. Y. Ivanov, and A. Stolow, J. Chem. Phys. **117**, 1575 (2004).
[5] M. Smits, C. A. de Lange, A. Stolow, and D. M. Rayner, Phys. Rev. Lett. **93**, 213003 (2004).
[6] T. Brabec, M. Cote, P. Boulanger, and L. Ramunno, Phys. Rev. Lett. **95**, 073001 (2005).
[7] Z. Zhao and T. Brabec, J. Phys. B **39**, L345 (2006).
[8] Z. Zhao and T. Brabec, J. Mod. Opt. **54**, 981 (2007).
[9] A. Kramida, Ralchenko, Yu., J. Reader, and NIST ASD Team, NIST atomic spectra database (version 5.3), National Institute of Standards and Technology, Gaithersburg, MD [http://physics.nist.gov/asd]
[10] X. Chu, A. Dalgarno, and G. C. Groenenboom, Phys. Rev. A **72**, 032703 (2005).
[11] G. C. Groenenboom, X. Chu, and R. V. Krems, J. Chem. Phys. **126**, 204306 (2007).
[12] X. Chu, A. Dalgarno, and G. C. Groenenboom, Phys. Rev. A **75**, 032723 (2007).
[13] X. Chu, Phys. Rev. A **82**, 023407 (2010).
[14] X. Chu and P. J. Memoli, Chem. Phys. **391**, 83 (2011).
[15] X. Chu and G. C. Groenenboom, Phys. Rev. A **87**, 013434 (2013).
[16] X. Chu and G. C. Groenenboom, Phys. Rev. A **93**, 013422 (2016).
[17] E. Runge and E. K. U. Gross, Phys. Rev. Lett. **52**, 997 (1984).
[18] E. K. U. Gross and W. Kohn, Adv. Quantum Chem. **21**, 255 (1990).
[19] G. Vignale, Phys. Rev. A **77**, 062511 (2008).
[20] X. Chu and M. McIntyre, Phys. Rev. A **83**, 013409 (2011).
[21] X. Chu and G. C. Groenenboom, Phys. Rev. A **85**, 053402 (2012).
[22] R. T. Sharp and G. K. Horton, Phys. Rev. **90**, 317 (1953).
[23] J. B. Krieger, Y. Li, and G. J. Iafrate, Phys. Lett. A **146**, 256 (1990).
[24] C. Lee, W. Yang, and R. G. Parr, Phys. Rev. B **37**, 785 (1988).
[25] X. M. Tong and S.-I. Chu, Phys. Rev. A **57**, 452 (1998).
[26] J. D. Ramsden and R. W. Godby, Phys. Rev. Lett. **109**, 036402 (2012).
[27] C. A. Ullrich, U. J. Gossmann, and E. K. U. Gross, Phys. Rev. Lett. **74**, 872 (1995).
[28] S. Raghunathan and M. Nest, J. Chem. Phys. **136**, 064104 (2012).